Article

Photoelectrochemical Studies on Metal-Doped Graphitic Carbon Nitride Nanostructures under Visible-Light Illumination

I. Neelakanta Reddy [1], N. Jayashree [2], V. Manjunath [3], Dongseob Kim [4],* and Jaesool Shim [1],*

[1] School of Mechanical Engineering, Yeungnam University, Gyeongsan 712749, Korea; neela.sra@gmail.com
[2] Department of Civil Engineering, National Institute of Technology, Mangalore 575025, India; jaymahi7777@gmail.com
[3] Department of Physics, Sri Padmavati Mahila Visvavidyalayam, Tirupati 517502, India; manjunathphy@gmail.com
[4] Aircraft System Technology Group, Korea Institute of Industrial Technology (KITECH), Cheonan 38822, Korea
* Correspondence: yusae@kitech.re.kr (D.K.); jshim@ynu.ac.kr (J.S.)

check for updates

Abstract: Recently, the engineering of optical bandgaps and morphological properties of graphitic carbon nitride (g-C_3N_4) has attracted significant research attention for photoelectrodes and environmental remediation owing to its low-cost synthesis, availability of raw materials, and thermal physical–chemical stability. However, the photoelectrochemical activity of g-C_3N_4-based photoelectrodes is considerably poor due to their high electron–hole recombination rate, poor conductivity, low quantum efficiency, and active catalytic sites. Synthesized Ni metal-doped g-C_3N_4 nanostructures can improve the light absorption property and considerably increase the electron–hole separation and charge transfer kinetics, thereby initiating exceptionally enhanced photoelectrochemical activity under visible-light irradiation. In the present study, Ni dopant material was found to evince a significant effect on the structural, morphological, and optical properties of g-C_3N_4 nanostructures. The optical bandgap of the synthesized photoelectrodes was varied from 2.53 to 2.18 eV with increasing Ni dopant concentration. The optimized 0.4 mol% Ni-doped g-C_3N_4 photoelectrode showed a noticeably improved six-fold photocurrent density compared to pure g-C_3N_4. The significant improvement in photoanode performance is attributable to the synergistic effects of enriched light absorption, enhanced charge transfer kinetics, photoelectrode/aqueous electrolyte interface, and additional active catalytic sites for photoelectrochemical activity.

Keywords: graphitic carbon nitride; kinetics; nickel; electrochemical impedance spectroscopy; photoelectrodes; photoelectrochemical activity

1. Introduction

Over the past few decades, energy and environmental issues have become the most important and popular topic worldwide. Compared to fossil fuels, hydrogen energy is ecofriendly and exhibits a higher calorific value, which is approximately four-fold higher than that of methane [1,2]. Hydrogen production from water has been attracting significant attention based on its potential to generate a clean energy carrier without CO_2 emissions [3]. Photoelectrochemical (PEC) water splitting is one of the most promising methods to produce pollutant-free hydrogen fuel [4,5]. Consequently, the development of novel, nontoxic, low-cost, efficient, and stable photoelectrodes is of great significance. To accelerate electron transfer, reduce electron–hole recombination, and improve the efficiency of hydrogen production, certain catalytic materials are essential, especially for future energy applications.

As a metal-free photocatalyst, graphitic carbon nitride (g-C_3N_4) has attracted significant interest owing to its remarkable physical and chemical properties, such as reliable thermal and chemical endurance, super hardness, high efficiency, stability, nontoxic photocatalysis, low density, water resistivity, and biocompatibility [6]. Thus, g-C_3N_4 is regarded as a promising semiconductor for surface modification, light-emitting devices, photocatalysis, and photoelectrodes, among others [7,8]. Of the various semiconductors investigated [9–12], g-C_3N_4 is characteristically nontoxic and metal-free, with a comparatively narrow bandgap (2.7 eV), high thermal and chemical stability, and attractive electronic properties. It is considered as a promising material owing to its reasonable bandgap and electron localization properties or appropriate microstructural active site anchoring with surface dissolution as well as nitrogen atom water-splitting defect [13,14]. Zhang et al. [15], in their study on band position, reported that the oxidation possibility of the conduction band and local valence band reduction are approximately 1.3 and 1.4 eV, respectively, which enhances oxygen reduction reaction, as determined by solar energy. Su et al. used g-C_3N_4 to comprehend alcohol oxidation in visible light [16]. Wang et al. [17] synthesized g-C_3N_4 for energy transducers. However, owing to the limitation of the visible-light response range, poor quantum efficiency, and low specific surface area, the real-time/practical applications of g-C_3N_4 remain unappreciated [6,18,19]. To improve the activity and enhance the absorption properties of g-C_3N_4, doping is considered as a versatile technique by many researchers [8,18,20,21]. Chai et al. observed an improved photocatalytic degradation of rhodamine B over P-doped g-C_3N_4 [22]. Dang et al. [23] produced photocatalytic hydrogen using a nickel-based catalyst combined with g-C_3N_4. Takanabe et al. [24] synthesized a MgPc/mpg-C_3N_4 photocatalyst to expand light absorption for the evolution of hydrogen. Recently, a Ni/g-C_3N_4 catalyst was designed for efficient ethanol electro-oxidation [25]. Gong et al. [26] developed NiO and Ni co-doped g-C_3N_4 for octylphenol sensing applications. It is evident that Ni-based g-C_3N_4 catalysts exhibit good catalytic activity; however, a methodical study on Ni-doped g-C_3N_4 photoelectrodes for PEC water-splitting activity remains unavailable. Hence, in the present study, we investigated the systematic variation of the Ni dopant effect on the structural, morphological, and optical properties of g-C_3N_4 as well as its PEC activity. The optimized 0.4 mol% Ni-doped g-C_3N_4 photoelectrode showed a noticeably improved PEC water-splitting activity. Additionally, the incorporation of Ni improved the photoanode performance and enhanced the charge transfer kinetics between the photoelectrode/aqueous electrolyte interface.

2. Results and Discussion

The crystalline structures of the synthesized pure and Ni-doped g-C_3N_4 nanostructures with various doping concentrations were examined via XRD (wavelength of 1.54060 Å), as shown in Figure 1.

The wide and highest intensity peak at 2θ = 27.37° is attributed to the (002) reflection of tri-s-triazine-based g-C_3N_4, which corresponds to the stacking of the conjugated aromatic system with an interplanar distance of 0.329 nm [27]. The XRD analysis of the pure g-C_3N_4 sample exhibited a hexagonal phase as per JCPDS: 87–1526. Furthermore, the XRD analysis of the Ni-doped g-C_3N_4 samples revealed that there were no characteristic peaks related to metallic nickel, nickel oxides (NiO and Ni_2O_3), nickel nitrides (Ni_3N), and nickel carbides (Ni_3C) in any of the Ni-doped g-C_3N_4 nanostructures, even at a high Ni dopant concentration of 0.5 mol%, which designates the substitution of Ni ions into the host g-C_3N_4 matrix, possibly in the form of Ni–N bonds due to the high affinity among the Ni^{2+} ions and negatively charged N atoms in the N pots of g-C_3N_4 [28]. The major peak intensity of Ni-doped g-C_3N_4 gradually decreased with increasing Ni dopant concentration, indicating that the deterioration of the (002) reflection plane was related to the inhibition of the polycondensation of g-C_3N_4 nanostructures upon increasing the dopant concentration of Ni. This is due to the hampering of polymeric compression, which breaks the lamellar structure, thereby resulting in a reduction in the crystallinity of g-C_3N_4 by increasing the Ni dopant concentration [29]. In addition, a slight shift in the (002) characteristic peak was observed for Ni-doped samples, indicating that the crystalline structure of the synthesized samples remained the same for the Ni dopant concentration. The abovementioned results indicate that the dopant was successfully incorporated into the host lattice

of the g-C$_3$N$_4$ nanostructures. Besides, catalytic materials with low crystallinity commonly have a larger number of defects that can trap a huge quantity of carriers, thereby leading to an enhancement of the photogenerated electron–hole separation rate. Meanwhile, the decrement in the interplanar positions could enable the passage of carriers between the stacked crystal planes [29]. All these advantages ensured improvement in the PEC performance.
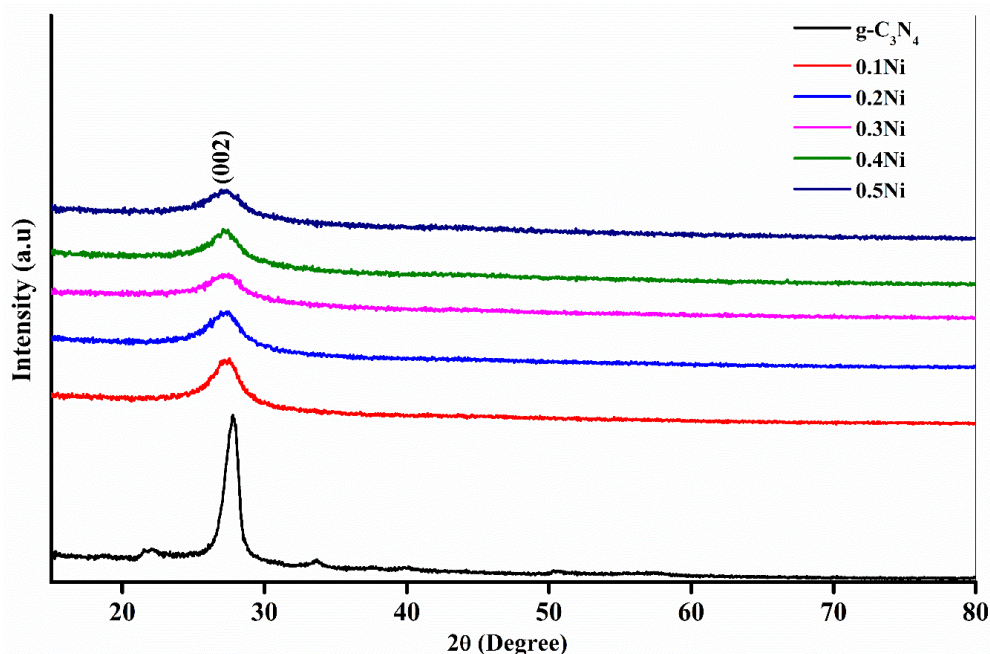

Figure 1. XRD analysis of pure and Ni-doped g-C$_3$N$_4$ porous nanosheets.

The distribution of elements in the synthesized samples were investigated using EDS analysis, as shown in Figure 2. The EDS analysis of the samples showed a uniform distribution of elements throughout the scanned area, indicating the quality of the prepared samples. As the concentration of dopant increased, the quantity of Ni incorporated into the host lattices also increased. This can be observed in the EDS mapping analysis of the synthesized samples.

The morphologies of the synthesized samples were investigated via TEM. Figure 3a–f shows the TEM images of the pure and Ni-doped g-C$_3$N$_4$ samples. All the samples exhibited a nanosheet-like morphology with an irregular porous appearance throughout the complete nanosheets.

Each pure and doped g-C$_3$N$_4$ photoelectrode nanosheet was several micrometers in length and nanometers in thickness. The porosity of the g-C$_3$N$_4$ nanosheets significantly increased with Ni dopant concentration. In addition, the nanosheets exhibited wrinkles and edge folds with increasing dopant concentration owing to the repulsion between the lone pair electrons at the N atom on the edge of the tri-s-triazine unit [30]. Xing et al. [31] observed a similar morphology for g-C$_3$N$_4$ nanosheets synthesized for H$_2$ evolution. However, changes in pore sizes and density were noticed with increasing dopant concentration, indicating that the dopant had a significant effect on the formation of porous nanosheets. Similar porous nanostructures have also been observed by several researchers [32,33]. The porous structure of photoelectrodes can offer a better surface area, improve the access to active sites, and charge pair separation and migration [33]. Furthermore, HR-TEM analysis was conducted for an optimized sample, i.e., 0.4 mol% Ni-doped g-C$_3$N$_4$ nanosheets, as shown in Figure 4a,b. The HR-TEM images indicated that the g-C$_3$N$_4$ nanosheets exhibited high porosity and edge folding, along with nanometers of thickness. The corresponding selected area electron diffraction (SAED) pattern is shown in the inset of Figure 4.
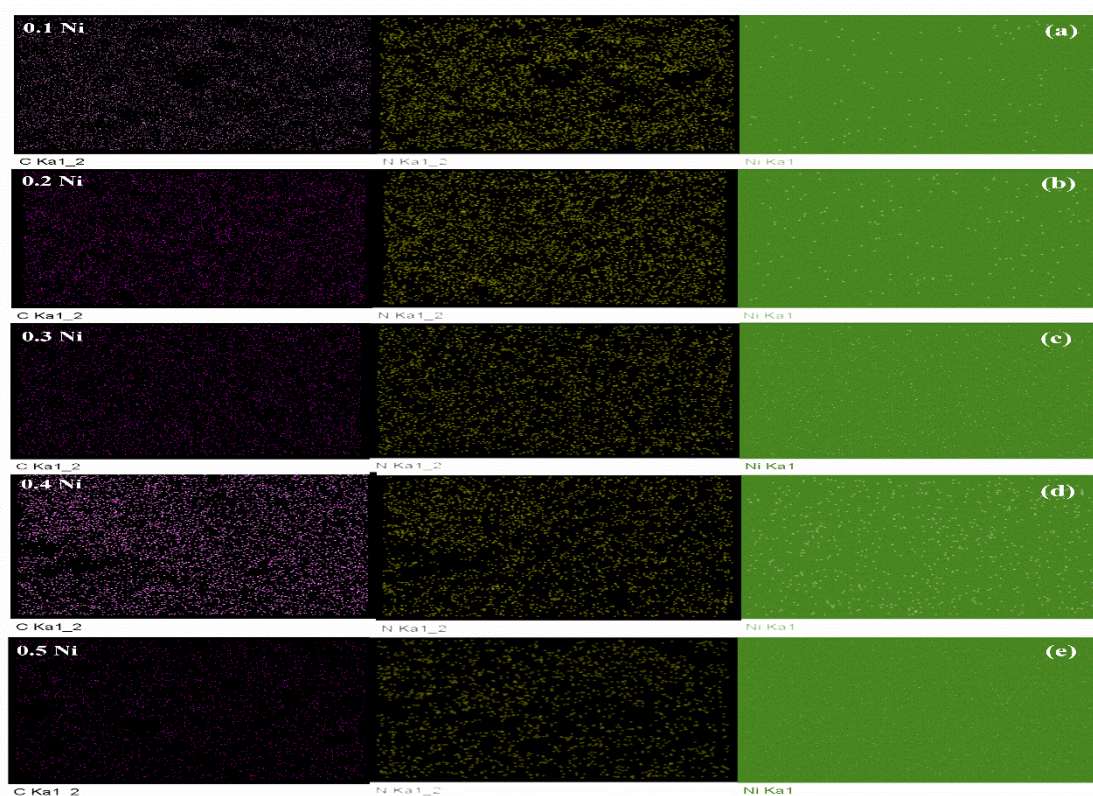
Figure 2. EDS images of synthesized photocatalysts: (**a**) 0.1 mol% Ni-doped g-C$_3$N$_4$, (**b**) 0.2 mol% Ni-doped g-C$_3$N$_4$, (**c**) 0.3 mol% Ni-doped g-C$_3$N$_4$, (**d**) 0.4 mol% Ni-doped g-C$_3$N$_4$, and (**e**) 0.5 mol% Ni-doped g-C$_3$N$_4$.
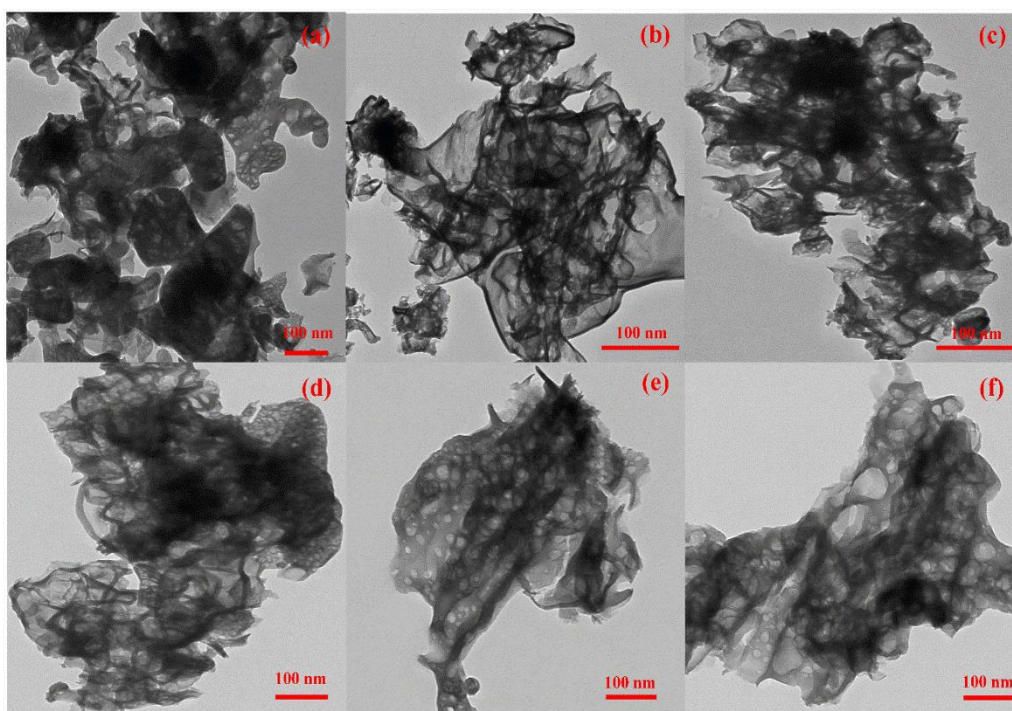
Figure 3. TEM images of synthesized photocatalysts: (**a**) pure g-C$_3$N$_4$, (**b**) 0.1 mol% Ni-doped g-C$_3$N$_4$, (**c**) 0.2 mol% Ni-doped g-C$_3$N$_4$, (**d**) 0.3 mol% Ni-doped g-C$_3$N$_4$, (**e**) 0.4 mol% Ni-doped g-C$_3$N$_4$, and (**f**) 0.5 mol% Ni-doped g-C$_3$N$_4$.
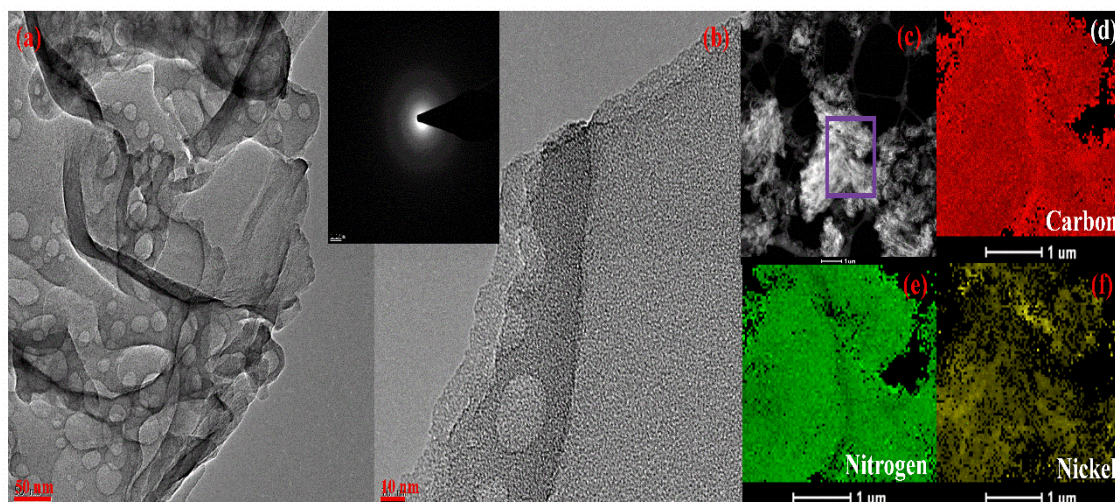
Figure 4. (**a**,**b**) HR-TEM images of optimized 0.4 mol% Ni-doped g-C$_3$N$_4$ nanosheets (inset: corresponding SAED) and (**c**–**f**) EDS images of optimized 0.4 mol% Ni-doped g-C$_3$N$_4$ nanosheets.

The ring SAED pattern corresponding to the (002) plane of g-C$_3$N$_4$ was observed for the optimized samples. From the abovementioned analysis, it is evident that the Ni dopant significantly affected the morphology of g-C$_3$N$_4$ and enhanced the PEC activity by improving the access to active sites. These results are consistent with the XRD analysis of the synthesized samples. Further, the EDS images of the optimized sample, shown in Figure 4c–f, indicated high uniform distribution of elements throughout the scanned area. This shows that the prepared catalysts had Ni dopant uniformly incorporated into the host structures.

The optical properties are important for determining the photocatalytic activity of the synthesized photoelectrodes. The absorption properties of pure and Ni-doped g-C$_3$N$_4$ were examined by UV–vis spectroscopy, as shown in Figure 5a–f, which revealed that the absorption edges of the pure and Ni-doped g-C$_3$N$_4$ photoelectrodes gradually shifted toward higher wavelengths with increasing dopant concentration.

The increase in the absorption edge may be due to the incorporation of the Ni dopant into the g-C$_3$N$_4$ host structures, thereby reducing the π-deficiency and causing imbalanced electron density in the π-electron conjugated systems [34,35]. A significant redshift along with increased absorption occurred for the Ni-doped g-C$_3$N$_4$ samples, which in turn enhanced the usage of the visible spectra. In addition, a slight peak at ~400 nm could be observed in Ni-doped g-C$_3$N$_4$ samples, perhaps due to the SPR (Surface Plasma Resonance) effect of the dopant, and occurred at a wavelength range of 390–540 nm depending on the Ni size. A similar increase in the absorption edge has also been observed by many researchers [21,36–38]. Furthermore, the optical bandgap of pure and Ni-doped g-C$_3$N$_4$ was estimated from the absorption spectra, as shown in Figure 6a–f. The corresponding estimated optical bandgap values were 2.53, 2.45, 2.28, 2.19, 2.18, and 2.22 eV, respectively, for the undoped and Ni-doped g-C$_3$N$_4$ samples.
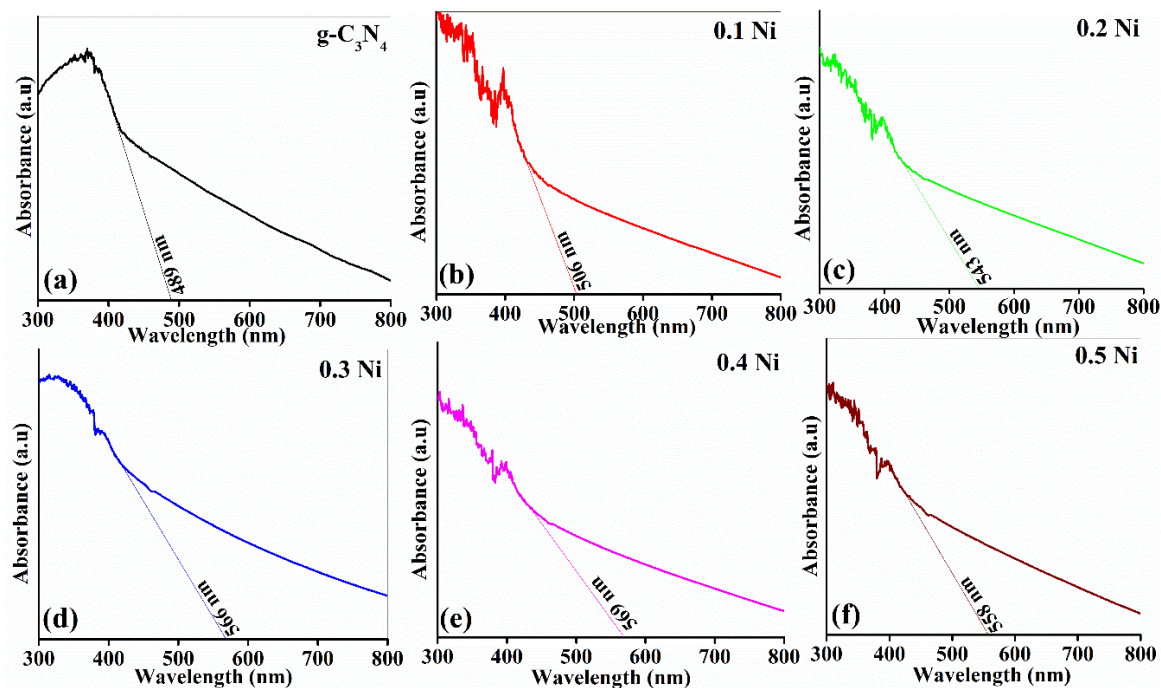
Figure 5. Absorbance spectra of synthesized photocatalysts: (**a**) pure g-C_3N_4, (**b**) 0.1 mol% Ni-doped g-C_3N_4, (**c**) 0.2 mol% Ni-doped g-C_3N_4, (**d**) 0.3 mol% Ni-doped g-C_3N_4, (**e**) 0.4 mol% Ni-doped g-C_3N_4, and (**f**) 0.5 mol% Ni-doped g-C_3N_4.
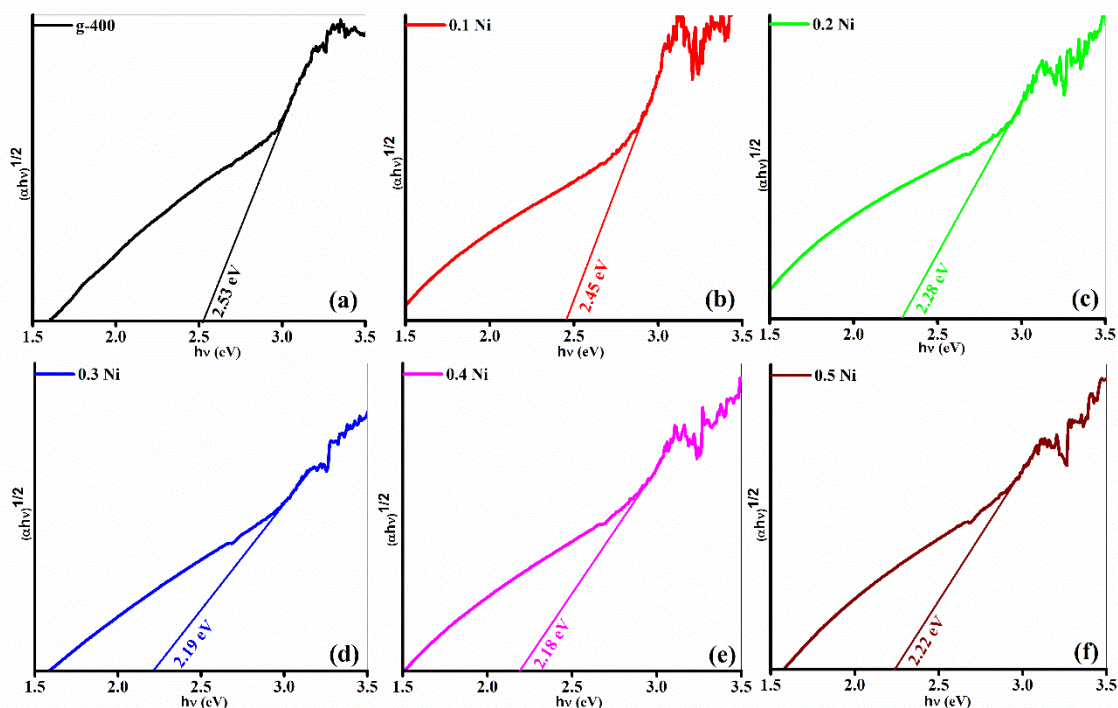
Figure 6. Optical bandgap vs. $(\alpha h\nu)^{1/2}$ curves for the synthesized photocatalysts: (**a**) pure g-C_3N_4, (**b**) 0.1 mol% Ni-doped g-C_3N_4, (**c**) 0.2 mol% Ni-doped g-C_3N_4, (**d**) 0.3 mol% Ni-doped g-C_3N_4, (**e**) 0.4 mol% Ni-doped g-C_3N_4, and (**f**) 0.5 mol% Ni-doped g-C_3N_4.

As the dopant concentration increased, the optical bandgap of g-C_3N_4 gradually decreased and shifted toward lower energies, thereby indicating that the Ni dopant was effectively incorporated into the g-C_3N_4 host structures. The incorporation of Ni dopant into the g-C_3N_4 host structures resulted in

a decrease in the bandgaps, which suggested a change in the electronic band structure upon Ni dopant substitution. The reduction of the optical band values may be due to the formation of intermediate states within the forbidden region. Owing to the presence of Ni dopant in the host g-C_3N_4 lattice, it is also possible that the localized isolated states of Ni formed below the conduction band (CB) minima and the dopant Ni atoms may form complexes, such as g-$C_3N_{4-n}Ni_n$, by utilizing the lone pairs of the neighboring nitrogen atoms, thereby resulting in a reduction in the bandgap [30]. Thus, the dopant Ni can shift the light absorption range of g-C_3N_4 from the UV to the visible region, leading to improved catalytic activity under solar radiation. Further, an increase of optical bandgap was observed for the 0.5 Ni sample, may be due to the Burstein–Moss (B–M) effect, which suggests that the optical band gap of degenerately doped semiconductors increases when all states close to the conduction band get populated due to shifting of an absorption edge to higher energy. The reduction in the g-C_3N_4 optical bandgap with various dopant concentrations has also been observed by many researchers [21,30,36–38]. This optical analysis indicates that the doped samples may generate more charges under visible irradiation, which can enhance the water-splitting activity compared to pure g-C_3N_4.

Superior generation, separation, and migration of energized charge pairs are essential for the PEC method; thus, to investigate the aforementioned properties, photoluminescence (PL) emission spectroscopy [32] was recorded at a wavelength of 325 nm. Figure 7a shows the PL spectra of the pure and Ni-doped g-C_3N_4 electrodes.

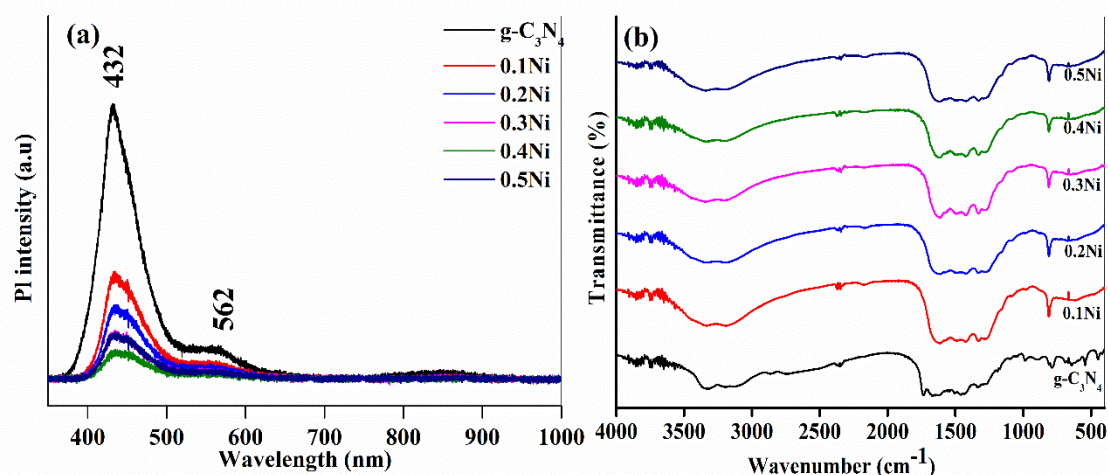**Figure 7.** (**a**) Photoluminescence spectra and (**b**) FTIR analysis of the synthesized photocatalysts.

The pure g-C_3N_4 exhibited two major emission peaks at 432 and 562 nm. The peak at 432 nm is ascribed to the recombination process of self-trapped excitons or excited charge pairs, which is used to approximate the transmission and separation efficiency of excited charge pairs, whereas the one at 562 nm is attributed to the neutral charge state of nitrogen vacancies [39–41]. The Ni-doped g-C_3N_4 electrodes also showed two similar major peaks at 432 and 562 nm. However, the intensity of these emission peaks decreased with increasing dopant concentration, and the emission peak positions were marginally shifted to higher wavelengths, thereby confirming the incorporation of dopants into the host g-C_3N_4 structures, which improved the separation of photoexcited charge carriers and significantly reduced the recombination rate of charge carriers. Furthermore, the g-C_3N_4 nanosheet-like nanostructures decreased the travel path distance of the generated charge pairs to the surface of the electrode, which diminished the recombination rate of the photoexcited charge carriers. The lowest charge recombination rate was observed in the 0.4 Ni sample, i.e., 0.4 mol% Ni-doped g-C_3N_4, compared to other photoelectrodes. Hence, optimal Ni-doped photoelectrodes may exhibit enhanced PEC activity compared to other photoanodes.

Figure 7b shows a FTIR analysis of all the synthesized photoelectrodes. The band appearing at ~810 cm^{-1} can be accredited to triazine breathing modes of CN heterocycles due to the s-triazine ring

systems [30] or an out-of-plane collective wagging vibration of the nitrogen and carbon atoms in the heptazine. The intense peaks originating between 1150 and 1650 cm^{-1} correspond to the stretching vibrations of CN heterocycles. The broad band at 3200 cm^{-1} is attributed to the stretching modes of the remaining uncondensed N–H groups due to inadequate polymerization, and the slight hump at 2169 cm^{-1} was due to the existence of cyano groups [30]. Due to dopant of Ni, the band at ~810 cm^{-1} remained unchanged. However, the dopant partially suppressed the aromatic CN heterocycles.

The chemical and electronic states of the synthesized pure and Ni-doped g-C_3N_4 nanosheet nanostructures were investigated via XPS analysis. The survey spectra between 0 and 1350 eV for all the photoelectrodes are shown in Figure 8. The spectra show only the existence of core elements, such as C, N, and Ni. The intensity of the dopant Ni peak increased with increasing dopant concentration in the host g-C_3N_4 nanostructures. No other impurities related to the metallic nickel peaks were observed, thereby indicating that the dopant had been incorporated into the host lattice. Similar XPS survey analyses were conducted on Ni-doped g-C_3N_4 for the degradation of methyl orange by Deng et al. [27].
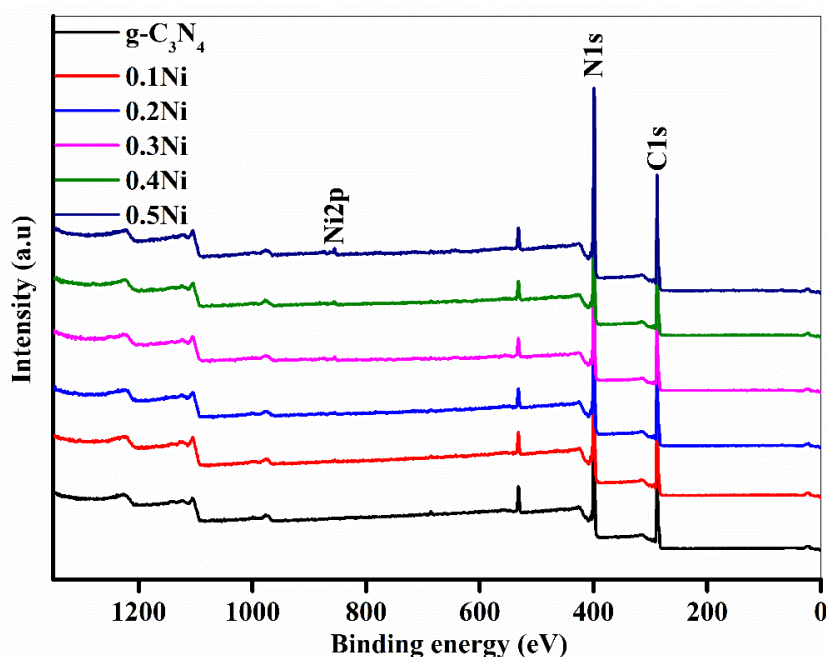
Figure 8. XPS survey spectra of pure and doped g-C_3N_4 nanosheets.

For more details, the core-level XPS spectra of C1s, N1s, and Ni2p were recorded to their respective binding energies. The high-resolution core spectra of the C1s peaks of all the synthesized photoelectrodes are shown in Figure 9a–f and resolved into two major peaks at ~288.0 and ~284.8 eV. The binding energy peak at ~284.8 eV relates to the sp^2 hybridized C–C bonds resulting from adventitious carbon, whereas that at ~288.0 eV is attributed to the sp^2-bonded carbon in the N–C=N tri-s-triazine rings of the elementary aromatic g-C_3N_4 cycles, which is the ruling carbon in the conjugated system. It was observed that the area of the peak of N–C=N coordination decreased with an increase in the Ni doping concentration, representing the alteration of the triazine rings [42].

The core-level spectra of the N1s peaks for all the pure and doped photoelectrodes are shown in Figure 10a–f, and they were deconvoluted into four major peaks at binding energies of 404.5, 400.8, 399.4, and 398.3 eV. The high-intensity peak centered at ~398.3 eV is attributed to the sp^2 hybridized aromatic N atoms bonded to carbon (N–C=N) [43], whereas that at 399.4 eV is ascribable to the sp^3 hybridized tertiary nitrogen N–$(C)_3$ groups [44]. These two types of nitrogen and carbon for N–C=N bonding were collected to build the heptazine heterocyclic ring (C_6N_7) style. The N1s peak was positioned at 400.8 eV, which is related to the shortened amino-functional clusters transporting hydrogen $((C)_2$–N–H) [44], while the weak peak at 404.5 eV is associated with the π excitation [44].
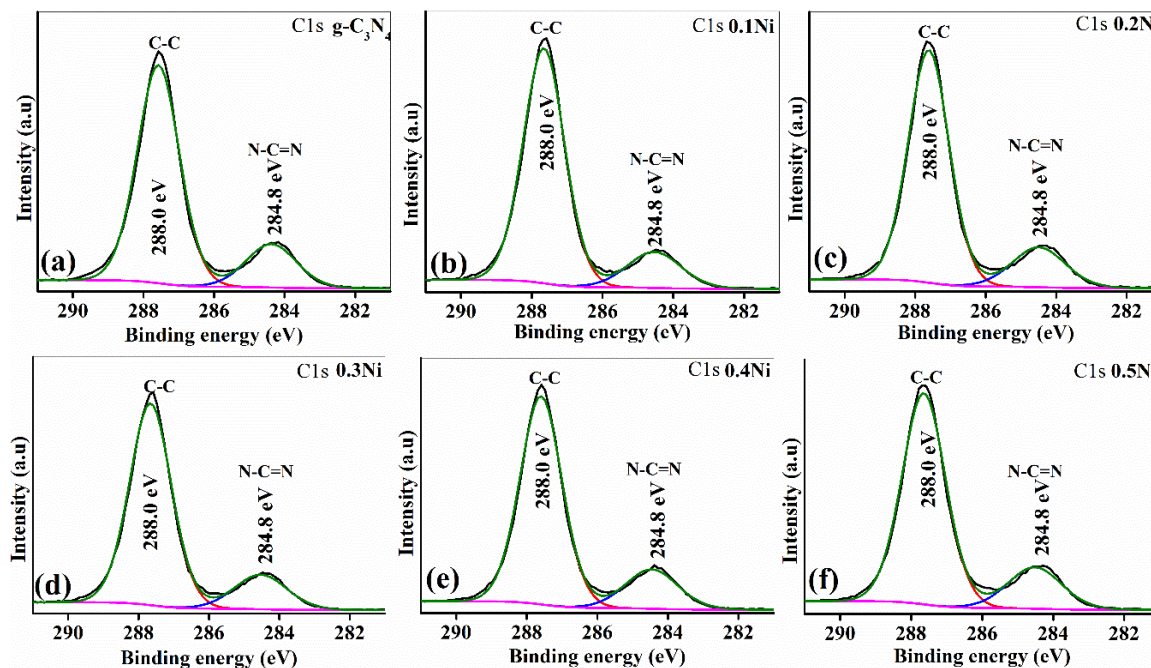
Figure 9. XPS core-level analysis of C1s: (**a**) pure g-C_3N_4, (**b**) 0.1 mol% Ni-doped g-C_3N_4, (**c**) 0.2 mol% Ni-doped g-C_3N_4, (**d**) 0.3 mol% Ni-doped g-C_3N_4, (**e**) 0.4 mol% Ni-doped g-C_3N_4, and (**f**) 0.5 mol% Ni-doped g-C_3N_4.
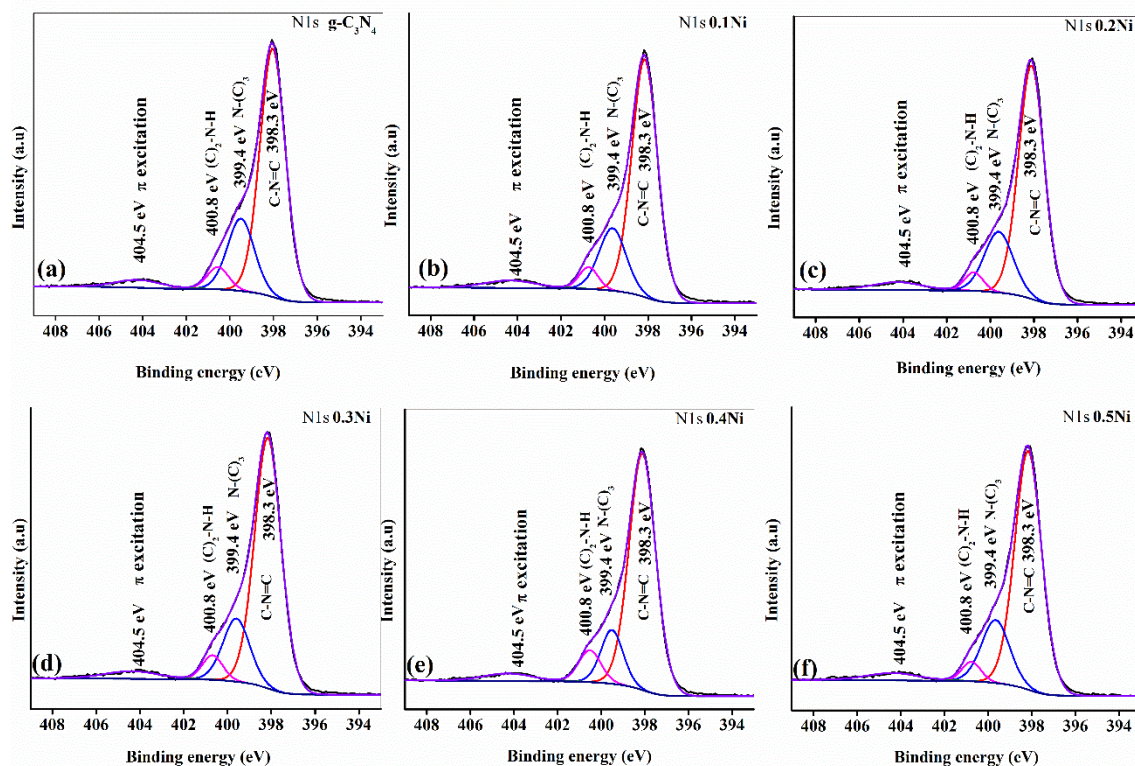
Figure 10. XPS core-level analysis of N1s: (**a**) pure g-C_3N_4, (**b**) 0.1 mol% Ni-doped g-C_3N_4, (**c**) 0.2 mol% Ni-doped g-C_3N_4, (**d**) 0.3 mol% Ni-doped g-C_3N_4, (**e**) 0.4 mol% Ni-doped g-C_3N_4, and (**f**) 0.5 mol% Ni-doped g-C_3N_4.

The core-level XPS spectra of Ni2p for the 0.1Ni, 0.2Ni, 0.3Ni, 0.4Ni, and 0.5Ni photoelectrodes are shown in Figure 11a–e. The corresponding concentration of Ni was 0.25, 0.35, 0.48, 0.55, and 0.63 at% for

0.1Ni, 0.2Ni, 0.3Ni, 0.4Ni, and 0.5Ni samples, respectively. All the Ni2p peaks contained four constituent peaks. These peak intensities increased with Ni dopant concentration in the g-C_3N_4 host structures. The main Ni2p peaks were located at binding energies of ~855.9 and 872.9 eV, which are attributed to $Ni2p_{3/2}$ and $Ni2p_{1/2}$ spin–orbits, respectively, and represent the characteristic bands of Ni^{2+} [45].
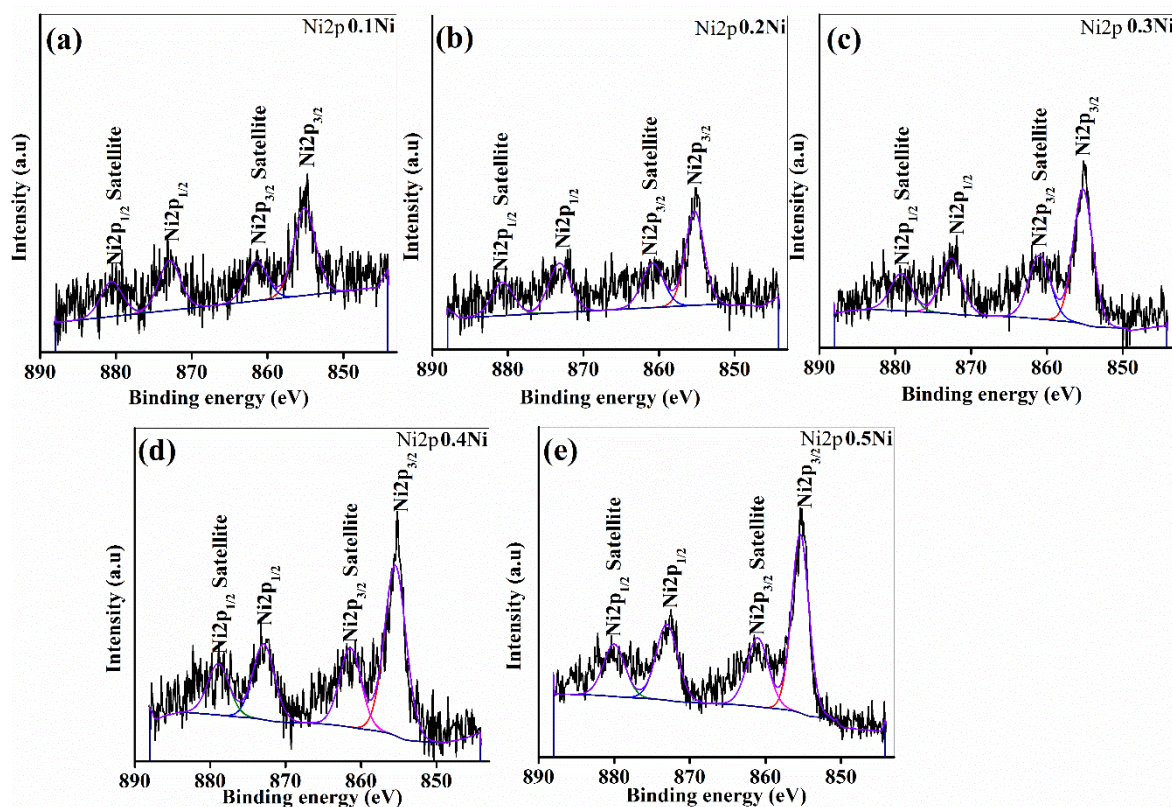
Figure 11. XPS core-level analysis of Ni2p: (**a**) 0.1 mol% Ni-doped g-C_3N_4, (**b**) 0.2 mol% Ni-doped g-C_3N_4, (**c**) 0.3 mol% Ni-doped g-C_3N_4, (**d**) 0.4 mol% Ni-doped g-C_3N_4, and (**e**) 0.5 mol% Ni-doped g-C_3N_4.

No characteristic metallic nickel peaks, such as those located at 852.9 and 870.3 eV for $Ni2p_{3/2}$ and $Ni2p_{1/2}$, respectively, were noticeable [46]. However, the peaks located at 861.6 and 879.9 eV are the satellite peaks of $Ni2p_{3/2}$ and $Ni2p_{1/2}$ for Ni^{2+}, respectively. These results reveal that Ni was present in the form of Ni^{2+} in all the Ni-doped samples. The abovementioned results are consistent with those reported in the literature [27,46].

For all the samples, valence band (VB) spectra were recorded to determine the VB positions, as shown in Figure 12. The VB energies for the doped g-C_3N_4 nanosheets were lower than those for the undoped g-C_3N_4 samples; the energies varied from 1.81 to 1.51 eV. The optical bandgaps obtained from the UV–vis spectroscopy analysis and the VB energies were used to determine the electronic structures and band locations of the synthesized photocatalysts, as illustrated in Figure 12. The Ni-doped g-C_3N_4 samples showed narrower optical bandgaps, high VB state potential, and low CB state potential as compared to the undoped g-C_3N_4 samples, enabling more efficient visible-light absorption and charge excitation and providing sufficient energy for water splitting. Accordingly, these photocatalysts are expected to demonstrate enhanced photoelectrode performance under visible-light irradiation for hydrogen generation.

For better PEC water-splitting activity, the photoelectrode should possess a low electrolyte and charge transfer resistance, high transport mechanism and charge separation rate, and good photoelectrode/electrolyte interface kinetics. The charge transfer resistances of the synthesized photoanodes were determined by electrochemical impedance spectroscopy via Nyquist plots in

0.1 M KOH aqueous electrolyte under visible-light illumination. The recorded Nyquist plots for all the photoelectrodes under light ON/OFF state are shown in Figure 13a.
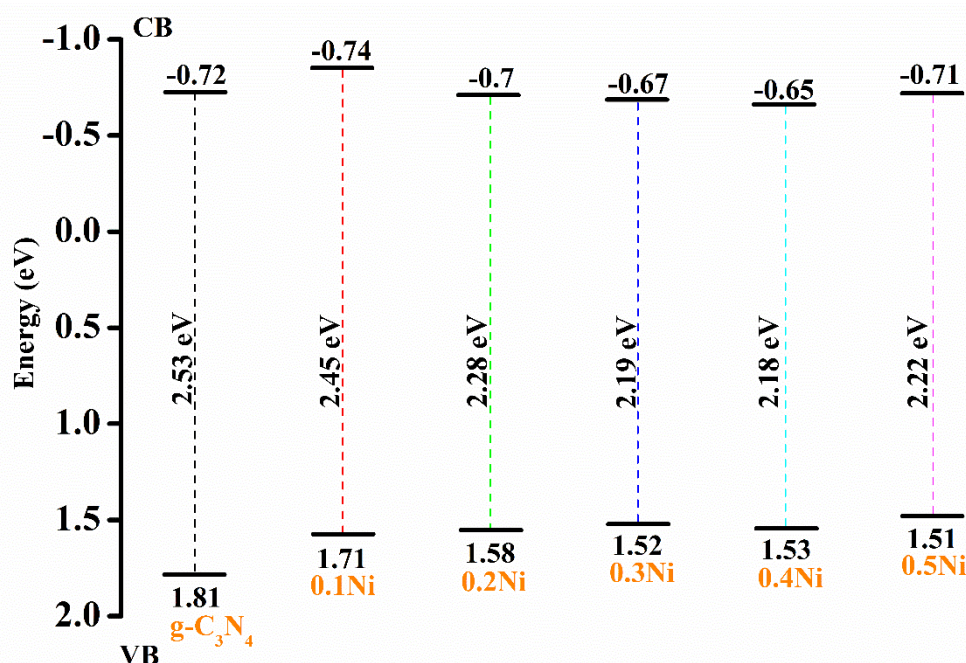

Figure 12. Band structures of pure and Ni-doped g-C$_3$N$_4$ photocatalysts.
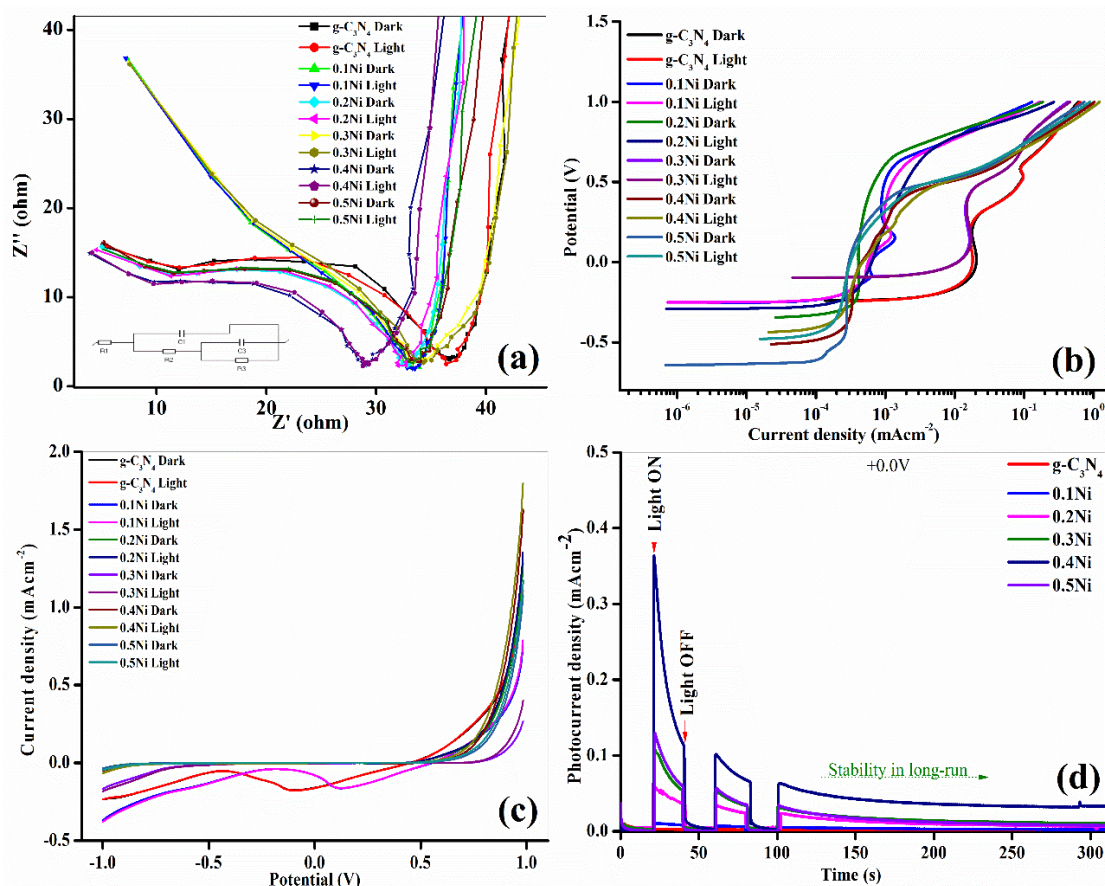

Figure 13. Photoelectrochemical water-splitting analysis of pure and doped g-C$_3$N$_4$ samples: (**a**) Nyquist plots, (**b**) Tafel plots, (**c**) linear sweep voltammetry, and (**d**) amperometry curves.

The obtained Nyquist plots were fitted with the equivalent circuits along with physical elements, as shown in the inset of Figure 13a. In the circuit, R1, R2, and R3 represent the solution resistance, ion-conducting path resistance, and the charge transfer resistance, respectively, whereas C2 and C3 represent the corresponding intact coating and double layer capacitances, respectively. The estimated physical element values under light ON/OFF states are listed in Table 1. Under both states, the solution resistance (R1) of all the synthesized samples was in the range of 0.13–1.01 Ω, indicating that all the photoelectrodes were compatible with the aqueous electrolyte, which could enhance charge migration between the electrode/electrode interface. The R3 values of the pure g-C_3N_4 photoelectrode under light ON/OFF were estimated to be 564.1 and 445.7 Ω, respectively, whereas the R3 values for the Ni-doped photoelectrodes drastically decreased with increasing Ni dopant concentration under both states. However, the R3 values of the doped photoelectrodes were much lower than those of the pure photoelectrode. The lowest R3 value of 81.2 Ω was obtained for the 0.4 mol% Ni-doped g-C_3N_4 photoanode under the light ON state. The R3 values seemingly followed the order of g-C_3N_4 > 0.1Ni > 0.2Ni > 0.3Ni > 0.4Ni < 0.5Ni, which confirmed that charge transfer between the electrode and aqueous electrolyte interface was very superficial. The above results suggest that the doping of Ni significantly improved the conductivity of the g-C_3N_4 nanostructures and considerably lowered the charge transfer resistance. Thus, the enhanced properties of Ni-doped g-C_3N_4 are attributable to the change in the g-C_3N_4 band structures and decrease in the charge transfer resistance. These results evidently show that the generated electron–hole pairs were better separated in the Ni-doped g-C_3N_4 photoelectrodes and that the interfacial charge transfer between the electron donor and acceptor was more efficient, resulting in a reduced recombination rate. In addition, the improved light absorption can be attributed to an increase in the number of photogenerated electron–hole pairs caused by doping, which consequently enhanced the PEC activity [47]. Therefore, the dopant significantly influenced the charge transfer properties of the host g-C_3N_4 photoelectrode, enhancing the electrochemical activity of the samples. To verify this assumption, the PEC properties of potentiodynamic, *I–V*, and *I–t* for all the synthesized photoelectrodes were recorded with a three-electrode setup in a 0.1 M KOH aqueous electrolyte under visible-light illumination.

Table 1. Nyquist plots fitted with equivalent circuit elements.

Same Name	*I–V* (mAcm^{-2})			Tafel Slopes (mVdec^{-1})	
	Dark	Light	ΔJ	Dark	Light
g-C_3N_4	1.078	1.107	0.029	92.1	91.2
0.1Ni	0.746	0.787	0.041	90.3	87.6
0.2Ni	1.283	1.352	0.069	85.7	81.2
0.3Ni	0.268	0.400	0.132	83.5	80.2
0.4Ni	1.630	1.797	0.175	79.3	76.0
0.5Ni	1.080	1.174	0.094	83.1	76.5

To understand the evolution reaction mechanism, the potentiodynamic analyses of all the synthesized g-C_3N_4-based photoelectrodes were investigated. The dynamic studies of pure and Ni-doped g-C_3N_4 photoelectrodes were recorded in a 0.1 M KOH aqueous electrolyte under light ON/OFF conditions, as shown in Figure 13b. The obtained Tafel plots were fitted with a Tafel equation, h = a + b log (j), to obtain the Tafel slopes for the pure g-C_3N_4 and Ni-doped g-C_3N_4 photoelectrodes. The estimated kinetic parameters from the Tafel fitting under light ON/OFF states are listed in Table 2.

Normally, the low Tafel slope values of the photoelectrodes indicate that the photoelectrode has a low applied potential to generate charge carrier pairs. However, these fitting and analysis should be interpreted carefully because the Tafel slopes differ in a complex manner depending on diverse constraints, such as reaction kinetics pathway, synthesis method, active site adsorption states, and catalyst type [48]. From Table 2, it can be seen that the Tafel slopes of the pure g-C_3N_4 photoelectrode exhibited a value of 92.1 and 91.2 mVdec^{-1} under light ON/OFF states, indicating that

the photoelectrode generated more carrier pairs under the light ON state. The Tafel slopes with various Ni dopant concentrations in the host g-C_3N_4 lattice evinced a significant effect on the Tafel slopes, whose values of doped photoelectrodes showed a decreasing trend with increasing Ni dopant concentration. The order of the Tafel slope values was as follows: g-C_3N_4 > 0.1Ni > 0.2Ni > 0.3Ni > 0.4Ni < 0.5Ni. However, the lowest Tafel slope value was obtained for the 0.4 mol% Ni-doped g-C_3N_4 photoelectrode compared to other synthesized photoanodes. In addition, the entire doped Tafel slope value was lower than that of the pure g-C_3N_4 photoelectrode, indicating that the doped electrodes required a lower applied potential than the pure g-C_3N_4 photoelectrode. From the abovementioned analysis, it is assumed that doped photoelectrodes may possess superior PEC performance.

Table 2. Photocurrents and Tafel slopes under light ON/OFF conditions.

Sample Name	State	R1 (Ω)	R2 (kΩ)	R3 (Ω)	C1 (nF)	C3 (μF)
g-C_3N_4	Dark	1.01	28.28	564.1	3.86	11.34
	Light	0.75	28.17	445.7	3.96	11.39
0.1Ni	Dark	0.86	33.69	236.8	1.76	9.41
	Light	0.68	33.51	220.3	1.93	9.24
0.2Ni	Dark	0.62	30.71	234.0	3.60	9.83
	Light	0.52	30.70	212.3	3.49	9.24
0.3Ni	Dark	0.75	35.69	134.7	1.75	7.56
	Light	0.66	34.16	128.2	1.74	7.73
0.4Ni	Dark	0.28	33.42	95.9	3.49	7.83
	Light	0.13	33.22	81.2	3.43	7.78
0.5Ni	Dark	0.67	31.10	130.5	3.48	6.62
	Light	0.64	31.06	114.3	3.46	6.83

The linear sweep voltammetry curves (*I–V*) of all the synthesized pure and Ni-doped g-C_3N_4 photoanodes were recorded in 0.1 M KOH electrolyte between the potentials of +1 and −1 V under light ON/OFF states, as shown in Figure 13c. All the voltammetry curves exhibited a general trend between the applied potentials. Extremely low photocurrents were observed for the pure g-C_3N_4 photoanode. The difference in photocurrents (ΔJ values) between the light ON and OFF states was approximately 0.029 mAcm^{-2} (Table 2). For Ni-doped g-C_3N_4 photoanodes, the photogenerated currents steadily increased with dopant concentration. The ΔJ values for the doped photoelectrodes are given in Table 2. However, the overall photocurrent generated from the doped photoelectrodes was higher than that from the pure g-C_3N_4 photoanode. The optimized photoelectrode of the 0.4 mol% Ni-doped g-C3N4 sample showed a maximum ΔJ value of 0.175 mAcm^{-2}, which is six-fold higher than that of the pure g-C_3N_4 photoelectrode. The order of photocurrents generated from the synthesized photoelectrodes was as follows: g-C_3N_4 < 0.1Ni < 0.2Ni < 0.3Ni < 0.4Ni > 0.5Ni. The enhanced higher photocurrent could be attributed to the appropriate charge transfer kinetics, structure, optical bandgap, and morphology of the 0.4Ni, i.e., 0.4 mol% Ni-doped g-C_3N_4 photoanode, compared to other photoanodes. This resulted in a low charge carrier migration path distance between the semiconductor photoelectrode and photoelectrode/aqueous electrolyte interface, higher charge transportation rate toward the solid/liquid interface, and improved charge collection [49]. The light absorption ability of the Ni-doped g-C_3N_4 photoelectrodes was considerably greater than that of the pure g-C_3N_4 photoelectrode, which resulted in enhanced electron–hole generation and separation. This could be due to the oscillation of light at larger frequencies, which encouraged electron–hole carrier pair generation. Consequently, electrons with sufficient energy impulsively drifted into the CB of the photoanode, then moved toward the Pt electrode, thus contributing to the improved PEC activity of the samples. Similarly, an energetic hole approached the photoelectrode/liquid electrolyte interface, whereby it oxidized water. Hence, the optimized Ni-doped g-C_3N_4 photoanode showed remarkably high photogenerated current value.

The amperometric curves (I–t) of the pure and Ni-doped g-C$_3$N$_4$ photoanodes are shown in Figure 13d. The pure Ni-doped g-C$_3$N$_4$ showed no switching phenomenon during light ON/OFF cycles and registered near-negligible photocurrents. However, the doped photoanodes exhibited an evident cycling behavior with increasing dopant concentration, which recorded significantly enhanced photocurrents. This indicates that the dopant significantly influenced the generation of photocurrents by the host g-C$_3$N$_4$-based photoanodes. All the doped samples showed higher photocurrents than the pure g-C$_3$N$_4$ during cycling as well as a long run-up of 310 s. The initial cycle of all the doped samples showed considerably higher photocurrents compared to consecutive cycles, possibly due to the availability of active sites in the host structures. These I–t results are consistent with the I–V, Nyquist, and potentiodynamic results. The stability of the photoelectrodes is determined by measuring the I–t curves for a long period of time; the initial portion of the I–t graph reveals that the switching behavior and stable photocurrents recorded for a long duration generates photoelectrode stability. Here, the stability of the synthesized photoelectrodes was tested up to 310 s, and all the photoanodes generated constant stable photocurrents during the long run, which indicated their high stability. The order of photocurrents generated by the photoanodes was as follows: g-400 < 0.1Ni < 0.2Ni < 0.3Ni < 0.4Ni > 0.5Ni. The above-stated I–t analysis indicates that optimal Ni doping into the host g-C$_3$N$_4$ lattices can efficiently enhance photocurrent generation. Thus, the superior PEC activities of Ni-doped photoelectrodes are ascribed to their efficient morphology, reduced bandgap, low electrolyte and charge transfer resistance, enhanced kinetics, and solid/electrolyte interface.

3. Experimental Section

3.1. Synthesis of g-C$_3$N$_4$ and Ni-Doped g-C$_3$N$_4$ Nanostructures

The direct calcination method was adopted to synthesize pure g-C$_3$N$_4$ and Ni-doped (i.e., Ni = 0.0, 0.1, 0.2, 0.3, 0.4, and 0.5 mol%) g-C$_3$N$_4$ nanostructures by weighing the stoichiometric ratio of urea and nickel nitrate hexahydrate (Ni(NO$_3$)$_2$ 6H$_2$O) materials. Typically, 10 g of urea and 0.1 mol% of Ni(NO$_3$)$_2$·6H$_2$O were thoroughly pulverized using a mortar and pestle for 1 h. Thereafter, the pulverized powder was transferred into a covered alumina crucible for heat treatment. All the samples were annealed at 400 °C in a muffle furnace for 2 h and then naturally cooled down to 25 °C upon the completion of the annealing process. Similarly, various molar concentrations of Ni were doped into the host g-C$_3$N$_4$ lattices by varying the stoichiometric amount of the Ni source material using the aforementioned procedure.

3.2. Preparation of Photoanodes

To prepare the g-C$_3$N$_4$-based photoanodes, 10 mg of each synthesized pure and Ni-doped g-C$_3$N$_4$ catalyst material was uniformly dispersed in 10 mL of ethylene glycol (C$_2$H$_6$O$_2$) via ultrasonication for 2 h. Next, the resultant solution was deposited on 1×1 cm^2 masked conductive indium tin oxide-coated glass substrates by a spin coater at 1500 rpm for 3 min. All the prepared photoanodes were dried at 120 °C in an oven for 12 h. Before deposition, the 2×1 cm^2 glass substrates were thoroughly cleaned with deionized water, ethanol (C$_2$H$_5$OH), and methoxyethane (C$_3$H$_8$O) for 30 min each using an ultrasonicator and dried in a vacuum oven at 100 °C for 1 h. These prepared photoanodes were considered as working electrodes for measuring the PEC properties of the synthesized samples.

3.3. Characterizations

The crystalline structures of the synthesized pure and Ni-doped g-C$_3$N$_4$ nanostructures were studied via X-ray diffraction (PANalytical, Almelo, The Netherlands), whereas transmission electron microscopy (TEM: TEM, Hitachi H-7600, Ibaraki, Japan) and high-resolution transmission electron microscopy (HR-TEM: HR-TEM, G2 F30 S-Twin, Hillsboro, OR, USA) were used to examine the morphology of the synthesized samples. The distribution of elements in the synthesized samples were examined by EDS attached with SEM (SEM: Hitachi S-4800, Ibaraki, Japan) and HR-TEM.

Ultraviolet–visible (UV–Vis: Neogen NEOD3117, Seoul, South Korea) spectroscopy was used to measure the absorbance and determine the optical bandgap of the samples. X-ray photoelectron spectroscopy (XPS) (Thermo Fisher Scientific MultiLab 2000, Seoul, South Korea) analysis was performed to investigate the chemical states, flat band potentials, and electronic structures of the samples.

3.4. Photocurrent, Potentiodynamic, and Impedance Measurements

The PEC properties, such as C–V, I–V, I–t, Tafel plots, and charge transfer kinetics, were investigated for g-C_3N_4-based photoelectrodes under visible-light ON/OFF conditions in a 0.1 M KOH aqueous electrolyte using a three-electrode Sp-200 Bio-Logic (Seyssinet-Pariset, rue de Vaucanson, France) potentiostat. Herein, the prepared photoanodes were utilized as the working electrodes, Pt wire as the counter electrode, and Ag/AgCl as the reference electrode. All the properties were measured with an AM 1.5G air mass filter, light source power density of 100 mWcm^{-2}, and UV cut-off filter ($\leq$400 nm, from Edmund optics Inc., Barrington, NJ, USA) focused on the 1 cm^2 photoanode. Furthermore, the Nyquist plots were recorded through electrochemical impedance spectroscopy for all the photoelectrodes at an amplitude of 5 mV in the applied frequency range of 5×10^6–100×10^{-3} Hz.

4. Conclusions

Herein, the engineering of optical bandgaps and morphological properties of g-C_3N_4 photoelectrodes for PEC water-splitting applications was successfully studied. It was observed that pure g-C_3N_4 photoelectrodes performed poorly because of their high electron–hole recombination rate and low charge transfer mechanism between the electrode/electrolyte interfaces. The synthesized Ni-doped g-C_3N_4 porous nanostructures improved light absorption. Additionally, a substantial effect on the structural and morphological properties of the g-C_3N_4 nanostructures was observed. The optical bandgap results varied from 2.53 to 2.18 eV with increasing Ni dopant concentration. Furthermore, a significant improvement in the electron–hole separation and charge transfer kinetics, which remarkably initiated enhanced PEC activity under visible-light irradiation, was observed. The optimized 0.4 mol% Ni-doped g-C_3N_4 photoelectrode exhibited considerably improved six-fold photocurrent density compared to pure g-C_3N_4.

Author Contributions: I.N.R.: Conceptualization, Methodology, Writing—Original draft preparation; N.J.: Written and analyzed optical data; V.M.: Written optical and structural data; D.K.: Funded generator, Investigation, Visualization; J.S.: Supervision, Writing—Reviewing and Editing. All authors have read and agreed to the published version of the manuscript.

Conflicts of Interest: The authors declare no conflict of interest.

References

1. Hu, Y.P.; Yan, X.Q.; Gu, Y.S.; Chen, X.; Bai, Z.M.; Kang, Z.; Long, F.; Zhang, Y. Large-scale patterned ZnO nanorod arrays for efficient photo electrochemical water splitting. *Appl. Surf. Sci.* **2015**, *339*, 122–127. [CrossRef]
2. Li, Z.S.; Luo, W.J.; Zhang, M.L.; Feng, J.Y.; Zou, Z.G. Photoelectrochemical cells for solar hydrogen production: Current state of promising photoelectrodes, methods to improve their properties, and outlook. *Energy Environ. Sci.* **2013**, *6*, 347–370. [CrossRef]
3. Hu, C.L.; Zhang, L.; Gong, J.L. Recent progress made in the mechanism comprehension and design of electrocatalysts for alkaline water splitting. *Energy Environ. Sci.* **2019**, *12*, 2620–2645. [CrossRef]
4. Kenney, M.J.; Gong, M.; Li, Y.G.; Wu, J.Z.; Feng, J.; Lanza, M.; Dai, H.J. High-performance silicon photoanodes passivated with ultrathin nickel films for water oxidation. *Science* **2013**, *342*, 836–840. [CrossRef]

5. Jacobsson, T.J.; Fjällström, V.; Edoff, M.; Edvinsson, T. Sustainable solar hydrogen production: From photoelectrochemical cells to PV electrolyzers and back again. *Energy Environ. Sci.* **2014**, *7*, 2056–2070. [CrossRef]

6. Zhang, J.; Zhang, G.G.; Chen, X.F.; Lin, S.; Dołega, L.; Mohlmann, G.; Lipner, G.; Antonietti, M.; Blechert, S.; Wang, X.C. Co-monomer control of carbon nitride semiconductors to optimize hydrogen evolution with visible light. *Angew. Chem. Int. Ed.* **2012**, *51*, 3183–3187. [CrossRef]

7. Shalom, M.; Gimenez, S.; Schipper, F.; Herraiz-Cardona, I.; Bisquert, J.; Antonietti, M. Controlled carbon nitride growth on surfaces for hydrogen evolution electrodes. *Angew. Chem. Int. Ed.* **2014**, *53*, 3654–3658. [CrossRef]

8. Nazarabad, M.K.; Goharshadi, E.K.; Mahdizadeh, S.J. Efficient photoelectrocatalytic water oxidation by palladium doped g-C_3N_4 electrodeposited thin film. *J. Phys. Chem.* **2019**, *123*, 26106–26115.

9. Ai, G.; Sun, W.T.; Gao, X.F.; Zhang, Y.L.; Peng, L.M. Hybrid CdSe/TiO_2 nanowire photoelectrodes: Fabrication and photoelectric performance. *J. Mater. Chem.* **2011**, *21*, 8749–8755. [CrossRef]

10. Wilker, M.B.; Shinopoulos, K.E.; Brown, K.A.; Mulder, D.W.; King, P.W.; Dukovic, G. Electron Transfer Kinetics in CdS Nanorod–[FeFe]-Hydrogenase Complexes and Implications for Photochemical H2 Generation. *J. Am. Chem. Soc.* **2014**, *136*, 4316–4324. [CrossRef]

11. Yu, J.; Jin, J.; Cheng, B.; Jaroniec, M. A noble metal-free reduced graphene oxide–CdS nanorod composite for the enhanced visible-light photocatalytic reduction of CO_2 to solar fuel. *J. Mater. Chem. A* **2014**, *2*, 3407–3416. [CrossRef]

12. Yang, X.; Cui, H.; Li, Y.; Qin, J.; Zhang, R.; Tang, H. Fabrication of Ag_3PO_4-graphene composites with highly efficient and stable visible light photocatalytic performance. *ACS Catal.* **2013**, *3*, 363–369. [CrossRef]

13. Zhang, Y.H.; Pan, Q.W.; Chai, G.Q.; Liang, M.R.; Dong, G.P.; Zhang, Q.Y.; Qiu, J.R. Synthesis and luminescence mechanism of multicolor-emitting g-C_3N_4 nanopowders by low temperature thermal condensation of melamine. *Sci. Rep.* **2013**, *3*, 1943. [CrossRef] [PubMed]

14. Tyborski, T.; Merschjann, C.; Orthmann, S.; Yang, F.; Lux-Steiner, M.-C.; Schedel-Niedrig, T. Tunable optical transition in polymeric carbon nitrides synthesized via bulk thermal condensation. *J. Phys. Condens. Matter.* **2012**, *24*, 162–201. [CrossRef]

15. Zhang, J.S.; Chen, X.F.; Takanabe, K.; Maeda, K.; Domen, K.; Epping, J.D.; Fu, X.Z.; Antonietti, M.; Wang, X.C. Synthesis of a carbon nitride structure for visible-light catalysis by copolymerization. *Angew. Chem. Int. Ed.* **2010**, *49*, 441–444. [CrossRef]

16. Su, F.Z.; Mathew, S.C.; Lipner, G.; Fu, X.Z.; Antonietti, M.; Blechert, S.; Wang, X. mpg-C_3N_4-Catalyzed selective oxidation of alcohols using O_2 and visible light. *J. Am. Chem. Soc.* **2010**, *132*, 16299–16301. [CrossRef]

17. Wang, X.C.; Maeda, K.; Thomas, A.; Takanabe, K.; Xin, G.; Carlsson, J.M.; Domen, K.; Antonietti, M. A metal-free polymeric photocatalyst for hydrogen production from water under visible light. *Nat. Mater.* **2009**, *8*, 76–80. [CrossRef]

18. Zhang, G.; Zang, S.; Wang, X. Layered Co (OH)$_2$ deposited polymeric carbon nitrides for photocatalytic water oxidation. *ACS Catal.* **2015**, *5*, 941–947. [CrossRef]

19. Shamsabadi, T.M.; Goharshadi, E.K.; Nazarabad, M.K. Z-scheme design of Ag@g-C_3N_4/ZnS photoanode device for efficient solar water oxidation: An organic-inorganic electronic interface, international journal of hydrogen energy. *J. Phys. Chem.* **2019**, *44*, 13085–13097.

20. Su, F.; Xu, C.; Yu, Y.; Zhang, W.D. Carbon self-doping induced activation of n–π* electronic transitions of g-C_3N_4 nanosheets for efficient photocatalytic H_2 evolution. *Chem. Cat. Chez.* **2016**, *8*, 3527–3535.

21. Wojtyła, S.; Śpiewak, K.; Baran, T. Doped graphitic carbon nitride: Insights from spectroscopy and electrochemistry. *J. Inorg. Organomet. Polym. Mater.* **2020**, *30*, 3418–3428. [CrossRef]

22. Chai, B.; Yan, J.; Wang, C.; Ren, Z.; Zhu, Y. Enhanced visible light photocatalytic degradation of Rhodamine B over phosphorus doped graphitic carbon nitride. *Appl. Surf. Sci.* **2017**, *391*, 376–383. [CrossRef]

23. Dong, J.F.; Wang, M.; Li, X.Q.; Chen, L.; He, Y.; Sun, L.C. Simple nickel based catalyst systems combined with graphitic carbon nitride for stable photocatalytic hydrogen production in water. *ChemSusChem* **2012**, *5*, 2133–2138. [CrossRef]

24. Takanabe, K.; Kamata, K.; Wang, X.; Antonietti, M.; Kubota, J.; Domen, K. Photocatalytic hydrogen evolution on dye-sensitized mesoporous carbon nitride photocatalyst with magnesium phthalocyanin. *Phys. Chem. Chem. Phys.* **2010**, *12*, 13020–13025. [CrossRef] [PubMed]

25. Graczyk, A.L.; Pieta, P.; Garbarino, G.; Busca, G.; Holdynski, M.; Kalisz, G.; Bartnicka, A.S.; Nowakowski, R.; Naushad, M.; Gawande, M.B.; et al. Graphitic carbon nitride–nickel catalyst: From material characterization to efficient ethanol electrooxidation. *ACS Sustain. Chem. Eng.* **2020**, *18*, 7244–7255. [CrossRef]

26. Gong, W.; Zou, J.; Zhang, S.; Zhou, X.; Jiang, J. Nickel oxide and nickel co-doped graphitic carbon nitride nanocomposites and its octylphenol sensing application. *Elctroanalysis* **2016**, *28*, 227–234. [CrossRef]

27. Deng, P.; Xiong, J.; Lei, S.; Wang, W.; Ou, X.; Xu, Y.; Xiao, Y.; Cheng, B. Nickel formate induced high-level in situ Ni-doping of g-C$_3$N$_4$ for a tunable band structure and enhanced photocatalytic performance. *J. Mater. Chem. A* **2019**, *7*, 22385–22397. [CrossRef]

28. Wang, X.; Chen, X.; Thomas, A.; Fu, X.; Antonietti, M. Metal-containing carbon nitride compounds: A new functional organic–metal hybrid material. *Adv. Mater.* **2009**, *21*, 1609–1612. [CrossRef]

29. Ma, T.; Shen, Q.; Zhao, B.; Xue, J.; Guan, R.; Liu, X.; Jia, H.; Xu, B. Facile synthesis of Fe-doped g-C$_3$N$_4$ for enhanced visible-light photocatalytic activity. *Inorg. Chem. Commun.* **2019**, *107*, 107451. [CrossRef]

30. Das, D.; Banerjee, D.; Mondal, M.; Das, N.S.; Ghorai, U.K.; Chattopadhay, K.K. Nickel doped graphitic carbon nitride nanosheeets and its application for dye degradation by chemical catalysis. *Mater. Res. Bull.* **2018**, *101*, 291–304. [CrossRef]

31. Xing, W.; Tu, W.; Han, Z.; Hu, Y.; Meng, Q.; Chen, G. Template-induced high-crystalline g-C3N4 nanosheets for enhanced photocatalytic H$_2$ evolution. *ACS Energy Lett.* **2018**, *3*, 514–519. [CrossRef]

32. Bao, N.; Hu, X.; Zhang, Q.; Miao, X.; Jie, X.; Zhou, S. Synthesis of porous carbon-doped g-C$_3$N$_4$ nanosheets with enhanced visible-light photocatalytic activity. *Appl. Surf. Sci.* **2017**, *403*, 682–690. [CrossRef]

33. Liang, G.; Waqas, M.; Yang, B.; Xiao, K.; Li, J.; Zhu, C.; Zhang, J.; Duanb, H. Enhanced photocatalytic hydrogen evolution under visible light irradiation by p-type MoS$_2$/n-type Ni$_2$P doped g-C$_3$N$_4$. *Appl. Surf. Sci.* **2020**, *504*, 144–448. [CrossRef]

34. Ho, W.; Zhang, Z.; Lin, W.; Huang, S.; Zhang, X.; Wang, X.; Huang, Y. Copolymerization with 2,4,6-Triaminopyrimidine for the rolling-up the layer structure, tunable electronic properties, and photocatalysis of g-C$_3$N$_4$. *ACS Appl. Mater. Interfaces* **2015**, *7*, 5497–5505. [CrossRef]

35. Qin, J.; Wang, S.; Ren, H.; Hou, Y.; Wang, X. Photocatalytic reduction of CO$_2$ by graphitic carbon nitride polymers derived from urea and barbituric acid. *Appl. Catal. B Environ.* **2015**, *179*, 1–8. [CrossRef]

36. Feng, J.; Zhang, D.; Zhou, H.; Pi, M.; Wang, X.; Chen, S. Coupling P nanostructures with P-doped g-C$_3$N$_4$ as efficient visible light photocatalysts for H$_2$ evolution and RhB degradation. *ACS Sustain. Chem. Eng.* **2018**, *6*, 6342–6349. [CrossRef]

37. Guo, Q.; Zhang, Y.; Qiu, J.; Dong, G. Engineering the electronic structure and optical properties of g-C$_3$N$_4$ by non-metal ion doping. *J. Mater. Chem. C* **2016**, *4*, 6839–6847. [CrossRef]

38. Xing, W.; Chen, G.; Li, C.; Han, Z.; Hu, Y.; Meng, Q. Doping effect of non-metal group in porous ultrathin g-C$_3$N$_4$ nanosheets towards synergistically improved photocatalytic hydrogen evolution. *Nanoscale* **2018**, *10*, 5239–5245. [CrossRef]

39. Ge, L.; Han, C.; Liu, J. Novel visible-light-induced g-C$_3$N$_4$/Bi$_2$WO$_6$ composite photocatalysts for efficient degradation of methyl orange. *Appl. Catal. B Environ.* **2011**, *108*, 100–107. [CrossRef]

40. Niu, P.; Zhang, L.; Liu, G.; Cheng, H.M. Graphene-like carbon nitride nanosheets for improved photocatalytic activities. *Adv. Funct. Mater.* **2012**, *22*, 4763–4770. [CrossRef]

41. He, K.; Xie, J.; Liu, Z.-Q.; Li, N.; Chen, X.; Hu, J.; Li, X. Multi-functional Ni$_3$C cocatalyst/g-C$_3$N$_4$ nano heterojunctions for robust photocatalytic H$_2$ evolution under visible light. *J. Mater. Chem. A* **2018**, *6*, 13110–13122. [CrossRef]

42. Chen, P.; Li, K.; Yu, Y.X.; Zhang, W. Cobalt-doped graphitic carbon nitride photocatalysts with high activity for hydrogen evolution. *Appl. Surf. Sci.* **2017**, *392*, 608–615. [CrossRef]

43. Zhang, G.; Huang, C.; Wang, X. Dispersing molecular cobalt in graphitic carbon nitride frameworks for photocatalytic water oxidation. *Small* **2015**, *11*, 1215–1221. [CrossRef]

44. Thomas, A.; Fischer, A.; Goettmann, F.; Antonietti, M.; Müller, J.O.; Schlögl, R.; Carlsson, J.M. Graphitic carbon nitride materials: Variation of structure and morphology and their use as metal-free catalysts. *J. Mater. Chem.* **2008**, *18*, 4893–4908. [CrossRef]

45. Berríos, C.; Cardenas-Jiron, G.I.; Marco, J.F.; Gutierrez, C.; Ureta-Zanartu, M.S. Theoretical and spectroscopic study of nickel(ii) porphyrin derivatives. *J. Phys. Chem.* **2007**, *111*, 2706–2714. [CrossRef] [PubMed]

46. Bi, L.; Xu, D.; Zhang, L.; Lin, Y.; Wang, D.; Xie, T. Metal Ni-loaded g-C$_3$N$_4$ for enhanced photocatalytic H2 evolution activity: The change in surface band bending. *Phys. Chem. Chem. Phys.* **2015**, *17*, 29899–29905. [CrossRef]

47. Huang, L.; Xu, H.; Li, Y.; Li, H.; Cheng, X.; Xia, J.; Xu, Y.; Cai, G. Visible-light-induced WO$_3$/g-C$_3$N$_4$ composites with enhanced photocatalytic activity. *Dalton Trans.* **2013**, *42*, 8606–8616. [CrossRef]

48. Liao, L.; Zhu, J.; Bian, X.; Zhu, L.; Scanlon, M.D.; Girault, H.H.; Liu, B. MoS$_2$ formed on mesoporous graphene as a highly active catalyst for hydrogen evolution. *Adv. Funct. Mater.* **2013**, *23*, 5326–5333. [CrossRef]

49. Wang, G.; Ling, Y.; Wheeler, D.A.; George, K.E.N.; Horsley, K.; Heske, C.; Zhang, J.Z.; Li, Y. Facile synthesis of highly photoactive α-Fe$_2$O$_3$-based films for water oxidation. *Nano Lett.* **2011**, *11*, 3503–3509. [CrossRef]